OPEN ACCESS
IOP Publishing
Journal of Physics B: Atomic, Molecular and Optical Physics
J. Phys. B: At. Mol. Opt. Phys. **57** (2024) 212002 (16pp)
https://doi.org/10.1088/1361-6455/ad7459

Topical Review

Ultralong-range Rydberg molecules

F B Dunning[1], **S K Kanungo**[1] and **S Yoshida**[2,*]

[1] Department of Physics and Astronomy, Rice University, Houston, TX 77005-1827, United States of America
[2] Institute for Theoretical Physics, Vienna University of Technology, Vienna, Austria

E-mail: shuhei@concord.itp.tuwien.ac.at

Received 2 February 2024, revised 7 May 2024
Accepted for publication 20 August 2024
Published 9 October 2024

Abstract

Ultralong-range Rydberg molecules (ULRMs) comprise a Rydberg atom in whose electron cloud are embedded one (or more) ground-state atoms that are weakly-bound through their scattering of the Rydberg electron. The existence of such novel molecular species was first predicted theoretically in 2000 but they were not observed in the laboratory until 2009. Since that time, interest in their chemical properties, physical characteristics, and applications has increased dramatically. We discuss here recent advances in the study of ULRMs. These have yielded a wealth of information regarding low-energy electron scattering in an energy regime difficult to access using alternate techniques, and have provided a valuable probe of non-local spatial correlations in quantum gases elucidating the effects of quantum statistics. Studies in dense environments, where the Rydberg electron cloud can enclose hundreds, or even thousands, of ground-state atoms, have revealed many-body effects such as the creation of Rydberg polarons. The production of overlapping clouds of different cold atoms has enabled the creation of heteronuclear ULRMs. Indeed, the wide variety of atomic and molecular species that can now be cooled promises, through the careful choice of atomic (or molecular) species, to enable the production of ULRMs with properties tailored to meet a variety of different needs and applications.

Keywords: ultralong-range Rydberg molecule, polaron, two-body correlation, rotational excitation, lifetime

1. Introduction

In 2000, Greene and coworkers [1] predicted theoretically the existence of an unusual ultralong-range molecular system that comprised a Rydberg atom in whose electron cloud is embedded a ground-state atom weakly-bound through scattering of the Rydberg electron from the ground-state atom [1–4]. This suggestion stimulated further theoretical interest, but it was not until 2009 that their existence was first demonstrated in the laboratory [2]. Since then, interest in these novel species has exploded with numerous studies of their chemical and physical properties, and their potential applications, being reported, and they remain the focus of much theoretical and experimental research. Much of the initial work in this area has been discussed in earlier reviews [3–8]. Therefore, we include here only a brief overview of this earlier work before focusing on areas not emphasized in these earlier reviews, on areas of recent interest, and on applications where the properties of these ultralong-range Rydberg molecules (ULRMs) are exploited. Whereas much of the early work focused on ULRMs involving alkali metal atoms, many more-recent experiments involve alkaline earth atoms.

* Author to whom any correspondence should be addressed.

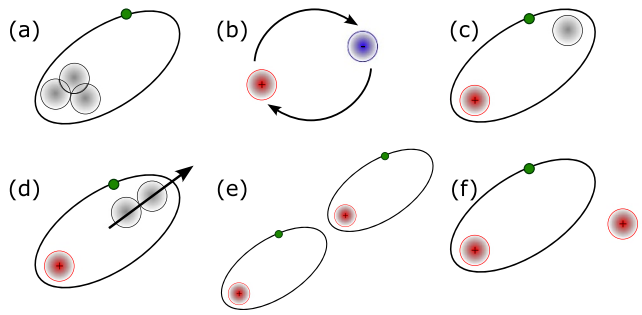

Figure 1. Schematic showing the different types of Rydberg-based long-range molecular systems. Positive ions are shown in red, negative ions in blue, neutral atoms (molecules) in gray, orbiting electrons as a green dot. (a) Molecule excited to a high-lying Rydberg state, (b) heavy-Rydberg ion-pair state, (c) ultralong-range Rydberg molecular dimer, (d) ultralong-range Rydberg molecule with a bound polar molecule, (e) ultralong-range Rydberg macrodimer, (f) bound Rydberg-ion pair.

1.1. Long-range molecular systems

ULRMs are only one of several classes of giant long-range Rydberg-based molecular systems, shown schematically in figure 1, that have been recently identified and studied. These include: giant molecules in which one electron is excited to a Rydberg state with a large principal quantum number, n [9]; heavy-Rydberg ion-pair states that comprise a positive-negative ion pair weakly bound by their electrostatic attraction (the molecular analog of a Rydberg atom) [10–18]; macrodimers made up of two Rydberg atoms bound at very large internuclear separations by their mutual interactions [19–23]; and long-range ion-Rydberg atom pairs bound by the interaction between the dipole moment induced in the Rydberg atom and the ionic charge [24–27].

All these different giant molecular species have one thing in common, they take advantage of the remarkable characteristics of Rydberg states [28, 29]. Foremost among these is their large physical size; their radii scale as n^2, and for values of $n \geqslant 100$ can exceed 1 μm. They are very fragile due to their small binding energies, $1/(2n^2)$ a.u., which are typically measured in meV to μeV. The electron orbits so far from the nucleus and remaining electrons, which together comprise a 'core ion' of unit positive charge, that the screened Coulomb field it experiences is very small. Its motion can therefore be strongly perturbed by the presence of even very weak external electric fields resulting in large polarizabilities and strong Stark effects. Indeed, even modest externally-applied fields can be sufficient to tear the electron from the atom leading to its ionization. Since the threshold for such field ionization, $1/(16n^4)$ a.u., is strongly dependent on n (and the projection m of orbital angular momentum l along the field axis), measurements of the product electrons or ions as a function of applied field provide a powerful detection and analysis tool in studies of Rydberg atoms and molecules [28–31].

ULRMs have provided a valuable microscale laboratory in which to study low-energy electron-atom scattering at energies not readily accessible using alternate techniques [32, 33], have furnished a powerful probe of non-local spatial correlations in cold quantum gases [34, 35], illuminating the important role played by quantum statistics. This implies that the ULRM formation is affected by the back ground gas of ground-state atoms. This coupling of a Rydberg atom or molecule dressed by the background gas provides the opportunity to study many-body phenomena, such as the creation of Rydberg polarons [36–39].

2. Theoretical description of ULRMs

2.1. Fermi pseudo-potential

The first studies of interactions between Rydberg- and ground-state atoms (or molecules) centered on the shifts and broadening of Rydberg levels [40–42]. Whereas it was initially expected that only red shifts would be observed due to dielectric screening of the Rydberg electron by the target gas, in certain cases blue shifts were observed. These surprising results were explained by Fermi using the 'essentially-free electron' model [28] which posits that, for sufficiently large values of n, in collisions with neutral targets a Rydberg atom behaves not as an atom, but as a pair of independent scatterers, the core ion and Rydberg electron. Fermi recognized that the observed behavior could be explained in terms of scattering of the quasi-free Rydberg electron from the target particle during a binary collision. He introduced two new concepts, the scattering length and the Fermi pseudopotential, that continue to play a critical role in low-energy physics [43]. Since, in high-n states, the average kinetic energy of the Rydberg electron, equal to its binding energy, is low, s-wave scattering plays a major role although, in certain cases, p- and higher-partial-wave scattering can be important. Fermi's theory was further developed by Omont who showed that the energy dependence of the s-wave scattering length must be taken into account when considering electron-neutral collisions [44]. The earliest line-shift and broadening experiments used classical absorption techniques but they were later extended to include laser-based measurements (see, for example, [45, 46]).

2.2. Diatomic ULRMs

The initial suggestion that ULRMs might be observed resulted from theoretical work by Greene *et al* [1] who recognized that the temperature and density of atoms in a Bose–Einstein condensate (BEC) were favorable for their creation. The ULRMs considered consisted of a dimer comprising rubidium Rydberg and ground-state atoms. The Rydberg atom was described using a single-active-electron model where the electron-ion core interaction was represented by the potential $V_c(r)$. For large internuclear separations the electron-ground-state-atom interaction is dominated by s-wave scattering and can be approximated by the Fermi pseudo-potential

$$V_s\left(\vec{r},\vec{R}\right) = 2\pi\, a_s\,(k)\,\delta\left(\vec{r}-\vec{R}\right) \qquad (1)$$

where $\vec{r}$ and $\vec{R}$ denote the electron and ground-state atom positions relative to the core ion, respectively, $a_s(k)$ the momentum-dependent scattering length and k is the momentum of the Rydberg electron relative to the ground state atom. (Atomic units are used throughout, unless otherwise noted.) After separating the center of mass motion of the molecule, the Hamiltonian of the Rydberg dimer can be approximated, in the limit of heavy atomic mass, to

$$H = \frac{P^2}{2\mu} + \frac{p^2}{2} + V_c(r) + V_{eg}\left(\vec{r} - \vec{R}\right) \tag{2}$$

where $\mu = m/2$ is the reduced mass for an atomic mass m, the potential V_{eg} can include both s- and p-wave scattering, and $\vec{p}$ and $\vec{P}$ are the electron and the ground-state atom momenta in the rest frame of the Rydberg ion core, respectively. Within the Born–Oppenheimer (BO) approximation and assuming that s-wave scattering is dominant, the electronic Hamiltonian can be written using the eigenstates $\langle\vec{r}|\varphi_{n,L,\Lambda}\rangle = \chi_{n,L}(r)Y_L^{\Lambda}(\hat{r})$ of an atom as

$$H_e = \sum_{n,L,\Lambda} E_{n,L}^{(0)} |\varphi_{n,L,\Lambda}\rangle\langle\varphi_{n,L,\Lambda}| + 2\pi\, a_s(k)\, |\Psi\rangle\langle\Psi| \tag{3}$$

with n the principal quantum number, L the orbital angular momentum, Λ the projection onto the (dimer) molecular axis, $E_{n,L}^{(0)}$ the energy of the Rydberg state, and $|\Psi\rangle = \sum_{n,L}\chi_{n,L}(R)Y_L^0(\hat{R})|\varphi_{n,L,0}\rangle$. This Hamiltonian implies that only molecular Σ states ($\Lambda = 0$) are affected by the presence of the ground state atom and admits two qualitatively different classes of electronic eigenstates. The first is associated with low-L Rydberg states with large quantum defects. The energy difference in the unperturbed energies $E_{n,L}^{(0)}$ is much larger than the off-diagonal coupling terms and the electronic state is largely unperturbed (see figure 2(a)). The resulting energy shift is, within the first order perturbation, given by

$$V_M(R) = \frac{a_s(k)}{2}(2L+1)\,|\chi_{n,L}(R)|^2. \tag{4}$$

The molecular BO potential displays a series of shallow minima (nearly invisible in the energy scale of figure 2) which accommodate only a small number of weakly-bound (~1-10 MHz) vibrational states that have relatively large internuclear separations. (Such states will be discussed in more detail later in connection with strontium ULRMs.)

The second class relates to nearly degenerate high-L states (i.e. $E_{n,L}^{(0)} \sim E_n^{(0)}$ for $L \geqslant L_{\min}$). The scattering by the ground-state atom couples different L levels but the interaction is too small to induce transitions to adjacent n levels. Therefore, the effective Hamiltonian becomes

$$H_e \simeq E_n^{(0)} \sum_{L,\Lambda} |\varphi_{n,L,\Lambda}\rangle\langle\varphi_{n,L,\Lambda}| + a_s(k) N_{s,\Sigma}^2 |\psi_{s,\Sigma}\rangle\langle\psi_{s,\Sigma}|. \tag{5}$$

The Σ states resulting from scattering by the ground-state atom

$$|\psi_{s,\Sigma}\rangle = \frac{1}{N_{s,\Sigma}} \sum_{L=L_{\min}}^{n-1} \sqrt{\frac{2L+1}{2}}\chi_{n,L}(R)\,|\varphi_{n,L,0}\rangle, \tag{6}$$

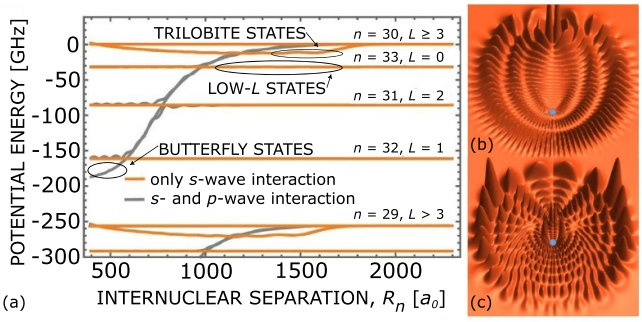

Figure 2. (a) Calculated BO potential energy curves for a rubidium ground state-Rydberg atom pair including only s-wave scattering (orange) and both s- and p-wave scattering (gray). Those regions responsible for the creation of low-L dimers, high-L 'trilobite' states, and 'butterfly' states (present only when including the p-wave shape resonance) are indicated ([4] [2020], reprinted by permission of the publisher (Taylor & Francis Ltd http://www.tandfonline.com)). Also included are electron probability distributions, in cylindrical coordinates, for (b) 'trilobite', and (c) 'butterfly' Rydberg dimers (Reproduced from [7]. © IOP Publishing Ltd All rights reserved. The position of the core ion is indicated by the blue dot.

with the normalization $N_{s,\Sigma} = (\sum_{L=L_{\min}}^{n-1}(L+1/2)(\chi_{n,L}(R))^2)^{1/2}$, are termed trilobite states because their associated electron probability density distributions, an example of which is shown in Figure 2(b), resemble the fossilized remains of such animals. The electronic state is related to an elliptic state [47] which is one representation of degenerate hydrogenic eigenstates. In essence, the distribution represents a superposition of all hydrogenic states that maximizes the electron density near the ground-state atom, providing it a small effective net negative charge that leads to its binding. The associated molecular BO potentials

$$V_M(R) = a_s(k) N_{s,\Sigma}^2 \tag{7}$$

show minima formed not only by the R-dependent electron wavefunctions in $N_{s,\Sigma}^2$ but also by the scattering lengths $a_s(k)$ that implicitly depend on R through the electron momentum $k(R)$. These minima are much deeper than for low-L states (see figure 2) and can support many more vibrational states with typical binding energies of a few tens of GHz. For homonuclear ULRM dimers, the gerade and ungerade electronic states are nearly degenerate due to their large bond length, and their superpositions can yield a permanent electric dipole moment which, for trilobite states involving many high-L levels, can be large [48].

At the smaller internuclear separations, where the classical electron momentum becomes larger, the effect of the p-wave scattering, described by

$$V_p\left(\vec{r},\vec{R}\right) = 6\pi\, a_p(k)^3 \overleftarrow{\nabla}\delta(\mathbf{r}-\mathbf{R})\overrightarrow{\nabla}, \tag{8}$$

where a_p is the p-wave scattering length, can become important [49]. The scattering potential becomes

$$V_p = a_p(k)^3 N_{p,\Pi}^2 |\psi_{p,\Pi}\rangle\langle\psi_{p,\Pi}| + a_p(k)^3 N_{p,\Sigma}^2 |\psi_{p,\Sigma}\rangle\langle\psi_{p,\Sigma}| \tag{9}$$

with

$$|\psi_{p,\Pi}\rangle = \frac{1}{N_{p,\Pi}} \sum_{L=L_{\min}}^{n-1} \sum_{\Lambda=1,-1} \frac{1}{2r} \sqrt{\frac{3L(L+1)(2L+1)}{2}} \times \chi_{n,L}(R) \left(-e^{i\phi}\delta_{\Lambda,1} + e^{-i\phi}\delta_{\Lambda,-1}\right) |\varphi_{n,L,\Lambda}\rangle \quad (10)$$

and

$$|\psi_{p,\Sigma}\rangle = \frac{1}{N_{p,\Sigma}} \sum_{L=L_{\min}}^{n-1} \sqrt{\frac{3(2L+1)}{2}} \chi'_{n,L}(R) |\varphi_{n,L,0}\rangle \quad (11)$$

with the normalization constants, $N_{p,\Pi}$ and $N_{p,\Sigma}$. Both Σ and Π states are perturbed by the p-wave scattering. The p-wave shape resonance present in electron-alkali atom scattering results in a rapid change in scattering phase near the resonance and substantially modifies the molecular BO potential surfaces. At small internuclear separations (see figure 2(a)) a deep minimum appears and couplings between the different BO surfaces leads to transitions between them and creation of more strongly-bound (~150 GHz) so-called butterfly states [49–51], again named for their electronic distributions (see figure 2(c)).

Theoretical models have been extended to ULRMs comprising alkaline earth atoms [52]. Whereas a p-wave shape resonance is predicted to be present for e-Mg scattering, no such resonances are expected for e-Sr and e-Ca scattering [53]. When the target Rydberg state is energetically far away from any doubly-excited 'intruder' states, the behavior of the Rydberg electron can be well approximated using a single-active-electron model. In the absence of p-wave resonances, the molecular levels can be analyzed within a single molecular BO surface as described earlier. However, for Ca the rapid changes in the quantum defect of 4*snd* states with n due to the presence of intruder states opens the possibility of mixing with other BO surfaces such as trilobite states [54].

2.3. Beyond the first order perturbation approximation

As discussed above, theoretical treatments of ULRMs frequently use a first-order perturbative approximation, in which the interaction of the Rydberg electron with the ground-state atom is represented through a zero-range Fermi pseudopotential. The scattering lengths, $a_s(0)$ and $a_p(0)$, (equations (1) and (8)) are typically used as fitting parameters to reproduce the measured ULRM vibrational levels. However, the values obtained frequently differ from those suggested by *ab initio* calculations of the scattering length for a collision between a free electron and the ground state atom.

In an attempt to solve this discrepancy, a number of alternate theoretical approaches have been implemented. For example, the BO molecular potential curves including the contributions from inelastic scattering can also be calculated non-perturbatively by evaluating the coupling between non-degenerate states. However, due to the singularity of the zero-range interaction, the calculation of BO potentials may not converge as the number of basis states increases [55]. An alternative method which circumvents the problems inherent in the zero-range potential, employs quantum defect theory [56] to calculate the BO potential surfaces [57, 58]. By combining with the local frame transformation, the local symmetry of the two scattering centers can be efficiently represented and the problem reduced to a boundary value problem in the asymptotic regime far from the scattering centers. This generalized local frame transformation (GLFT) provides results that differ somewhat from those obtained using a perturbative approach, in particular for the high-L trilobite or butterfly states of rubidium. However for low-L strontium Rydberg dimers, these differences are only large near the dissociation threshold, where the semiclassical approximation of the collision momentum k breaks down. The scattering lengths a_s and a_p derived from the experimental data using the GLFT approach show similar discrepancies to the values predicted by *ab initio* calculations. GLFT theory, however, can be extended to Rydberg atoms in the presence of multiple perturbers or to cases where the perturber is a molecule. It can also be combined with other frame transformations to investigate more complex situations such as Rydberg molecules in an electric field or inclusion of relativistic effects. Another theoretical approach involves full spin-dependent Green's functions [59] in which the BO surfaces are obtained by numerical solution of the roots of a determinantal equation. The method, which can be applied to any combination of alkali metals, eliminates the ambiguity associated with the non-convergent diagonalization approach.

For non-hydrogenic atoms, the trilobite and butterfly states involve the coupling between non-degenerate L states. Inelastic scattering of the Rydberg electron can transfer energy to the ground state atom and induce diabatic transitions between different BO potential surfaces [50] (see also section 9). A theoretical model to describe the diabatic transitions between different vibronic BO surfaces has been developed [51, 60]. The method demonstrates a non-negligible probability for diabatic transitions between the high-L molecular states and further suggests energy shifts in the potential surfaces due to the Born–Huang approximation.

2.4. Rotational states

The rotational excitation of Rydberg molecules provides another avenue to study the effects of Rydberg electron scattering from a ground state atom. Due to the rotational invariance of the original three-body Hamiltonian (equation (2)) the total orbital angular momentum $\vec{K} = \vec{L} + \vec{N}$ of the Rydberg electron $\vec{L}$ and the rotational angular momentum $\vec{N}$ of the molecule is preserved. Using the total angular momentum basis, the Hamiltonian for the vibrational motion of a Rydberg dimer becomes [61]

$$H_M = \frac{P_R^2}{2\mu} + \frac{K(K+1) + \langle L^2 \rangle - 2\Lambda^2}{2\mu R^2} + V_M(R)\,. \quad (12)$$

where μ is the reduced mass. For the low-L Rydberg dimers the mixing of L levels is negligible. The cylindrical symmetry

also preserves the projection Λ. Therefore, the ULRM can be characterized by the quantum numbers K, L and Λ. The expectation value can be evaluated as $\langle L^2\rangle = L(L+1)$. Given the absence of spin–orbit coupling for S states (Hund's case (b)) the total spin S is also a good quantum number. The total angular momentum K_S including the spin angular momenta (i.e. $\vec{K}_S = \vec{K} + \vec{S}$) replaces K when the molecular spin–orbit coupling is non-negligible. For the other low-L ULRMs the fine structure splittings dominate over the interaction with the perturber atom (Hund's case (c)) and ULRMs are characterized by the quantum numbers, K_S, L and Ω (the projection of $\vec{J} = \vec{L} + \vec{S}$ onto the molecular axis) [62].

For trilobite states involving states with large values of L the exchange of angular momentum through collisions between the Rydberg electron and the ground state atom can be sizable. The centrifugal energy for $n = 30$, $K = 0$ (i.e. $N = L$), and $\Lambda = 0$ ranges a few MHz at $R \sim 2n^2$ to 100 MHz at $R \sim n^2/2$ since the expectation value $\langle L^2\rangle = \langle \psi_{s,\Sigma}|L^2|\psi_{s,\Sigma}\rangle$ is R-dependent. However, the energy scale of the vibrational motion is larger than 1 GHz near the bottom of the molecular potential well. Additionally, the vibration wavefunctions are typically well localized in space and the the centrifugal energy results in a constant energy shift which is often neglected. As L increases the spin–orbit coupling becomes comparable to, or smaller than, the scattering interaction. In the limit that the spin–orbit coupling becomes smaller than the rotational energy, the molecule can be characterized by the quantum numbers Λ, S and K_S (Hund's case (b)).

3. Experimental realizations of Rydberg molecules

Early experimental studies of ULRMs were undertaken using alkali metals. Their first direct experimental observation was made by Pfau and co-workers using an ultracold sample of ^{87}Rb atoms and two-photon photoassociation [2]. These initial studies involved S states and demonstrated the production of weakly-bound ULRMs in both the ground and first excited vibrational levels. Measurements were extended to include more-highly-excited vibrational states and the formation of Rydberg trimers [63]. In later studies the formation of tetramers and pentamers was seen [64]. ULRM creation using P [65, 66] and D [67, 68] states has also been reported. Trilobite dimer states were created in ^{133}Cs by exploiting the near integer value of the S state quantum defect ($\delta = 4.05$) [69]. This leads to strong admixing of the nS state with the neighboring manifold of degenerate high-ℓ, $(n-4)\ell$, states thereby facilitating the formation of trilobites with kilodebye permanent electric dipole moments [70]. The production of pendular butterfly states during excitation in a weak electric field was also examined [71]. ULRMs were shown to provide a valuable probe of electron-atom (molecule) s-wave scattering lengths, and the shape of the p-wave resonance [32].

Measurements were extended to include the alkaline earths such as strontium [52]. The even strontium isotopes, ^{84}Sr ^{86}Sr and ^{88}Sr have no nuclear spin and for ULRMs involving an nS Rydberg state, spectral complexities associated with the Rydberg electron spin-orbit and ground-state hyperfine interactions (and with the p-wave shape resonances present in electron-alkali-atom scattering [53]) are absent. They have optically-active core ions allowing their detection through fluorescence or autoionization [72, 73]. Furthermore, for strontium the atom-atom s-wave scattering lengths span an unusually broad range of values (see table 1) admitting new opportunities for their application. They also feature narrow-linewidth intercombination lines which allow direct cooling to temperatures of a few microkelvin in a magneto-optical trap (MOT) and facilitate experiments employing Rydberg dressing [74]. The creation of ^{84}Sr ULRM dimers was first detected through ground-state atom loss from a trap [52] and again could be well described using a Fermi pseudopotential that incorporated both s- and p-wave scattering.

Table 1. Atom-atom s-wave scattering lengths for different strontium isotope combinations expressed in terms of the Bohr radius, a_0. Their natural abundances are also shown.

	^{84}Sr	^{86}Sr	^{87}Sr	^{88}Sr	Abundance (%)
^{84}Sr	123	32	−57	1700	0.56
^{86}Sr	32	811	162	97	9.86
^{87}Sr	−57	162	96	55	7.00
^{88}Sr	1700	97	55	−2	82.58

4. Probing anion properties using ULRMs

ULRM formation has been exploited to make detailed studies [33] of the negative ion shape resonance present in e-Rb scattering and the underlying Rb^- anion states [75]. Analysis of the measured binding energies of Rb($35S_{1/2}$) - Rb($5S_{1/2}$) dimers allowed extraction of s- and p-wave scattering lengths as well as the resolution of the ^3P_J fine structure manifest in the Rb^- anion which results from spin–orbit coupling and introduces three different p-wave scattering channels. These were explored using deeply-bound 'butterfly' dimer states which have substantial p-wave scattering character. This resulted in a doublet structure whose behavior in an applied magnetic field was also examined. The data were interpreted using detailed theory in which the anion fine structure enters through three J-dependent p-wave scattering channels. A more recent study of spin-orbit interactions utilized Rb($16P_{3/2}$) - Rb($5S_{1/2}$) dimers and spin-polarized Rydberg atoms [76]. Three vibrational ladders of molecular Rydberg states were observed, each of which displayed characteristic line-multiplet substructure, allowing for unambiguous assignment of all spin states. The results were in good agreement with model calculations that included spin-orbit and spin-spin interactions.

A dressed ion-pair model can also be used to model the behavior of ULRMs [77]. As noted earlier, in a heavy-Rydberg ion-pair state an atomic ion replaces the Rydberg electron to create an $A^+ \ldots B^-$ bound molecule [10–18]. In a trilobite ULRM (or other molecules involving high-L atomic Rydberg states) the electron wavefunction is localized near the neutral perturber (see figure 2). The neutral atom dressed by the

electronic charge is then viewed as forming an anion of fractional charge. Although this ignores the total trilobite wave function except for that part localized by the electron-neutral interaction, it provides a nice intuitive picture of ULRM binding. For $L \geqslant 2$, the effective anion charge was found to be nearly independent of the internuclear separation, R, resulting in a Coulomb-like interaction. In applying this model to rubidium dimer ULRMs, the corresponding potential curves were calculated using a GLFT approach, the triplet electron-neutral phase shifts being obtained from a non-relativistic two-electron R-matrix code. The results capture the emergence of the Coulomb character of the potential energy curves as L is increased and highlight the differences between these and those for the S and P states. A new series of vibrational states was identified which form a trimmed heavy-Rydberg series with very small Rydberg constant. Similar series are to be expected in any system comprising a Rydberg atom and polarizable perturber. Interestingly, studies of Cs(nD_J)-Cs($6S_{1/2}$) trilobite molecules point to negative dipole moments, i.e. a deficiency in the Rydberg electron density near the ground-state perturber, that is caused by electronic configuration mixing [78].

5. Probing non-local spatial correlations in quantum gases

Studies of non-local spatial correlations exploit the characteristics of the Born–Oppenheimer molecular potential for a low-L Rydberg atom-ground state-atom pair. Figure 3 shows such a potential for a strontium Sr($5s31s$) - Sr($5s^2$) atom pair calculated using a Fermi pseudopotential that includes both s- and p-wave scattering, together with the corresponding vibrational levels and wavefunctions. Due to a negative scattering length $a_s(0)$, the potential mirrors the electron probability density distribution (equation (4)) with a deep minimum near the outer classical turning point. The ground vibrational state is strongly localized in the outermost potential well and has a well-defined bond length at $R = R_n$ of $\sim 1.8(n-\delta)^2$ a.u., where the quantum defect δ for $^3S_1$ states is $\delta \simeq 3.371$.

The rate for photoassociation of a Rydberg dimer state is

$$P_{\nu,L,K} = \left|\langle\varphi_{n,L,0}|d^{(2)}|g\rangle F_\alpha(\nu,L,K)\right|^2 . \tag{13}$$

Since the electronic state of nS ULRMs is largely unperturbed, the two-photon transition $\langle\varphi_{n,L,0}|d^{(2)}|g\rangle$ is given by that for an isolated atom between the ground, $|g\rangle$, and Rydberg, $|\varphi_{n,L,0}\rangle$, states. The Franck–Condon factor ($K = N$ for $L = 0$)

$$F_\alpha(\nu = 0, L = 0, N) = \langle\nu, L = 0, N|\alpha\rangle \tag{14}$$

provides the overlap between the initial two-body scattering wavefunction $|\alpha\rangle$ in the ultracold gas (α represents a set of quantum numbers characterizing the scattering state) and the ULRM $|\nu, L = 0, N\rangle$. For the ground vibrational state ($\nu = 0$) localized at $R \simeq R_n$ the excitation rate serves as a measure of the relative probability of initially having two atoms with separation R_n in the initial gas. The pair correlation function

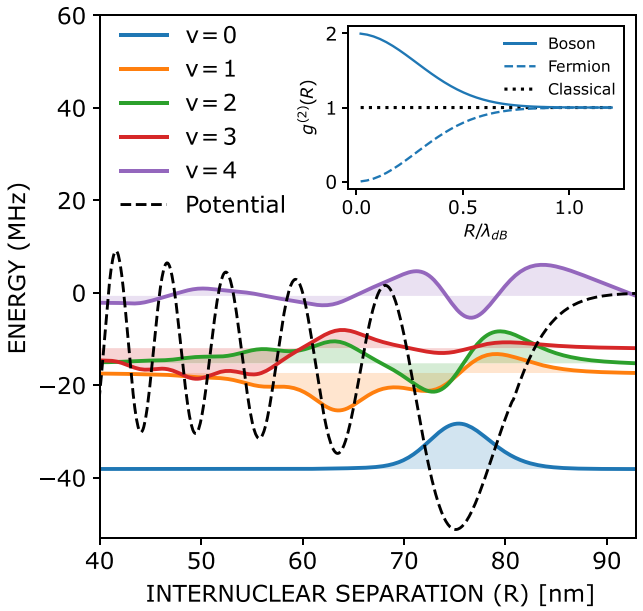

Figure 3. Calculated BO molecular potential for a $5s31s\ ^3S_1$-$5s^2\ ^1S_0$ strontium atom pair. The calculated vibrational wavefunctions multiplied by R are included. The horizontal axis for each indicates its binding energy. The inset shows the calculated values of $g^{(2)}(R)$ as a function of $R/\lambda_{\rm dB}$ for a gas of indistinguishable bosons, of indistinguishable fermions, and a classical gas.

$g^{(2)}(\vec{R})$ of the initial ultracold gas is the ensemble average of these two-body wavefunctions, i.e.

$$g^{(2)}\left(\vec{R}\right) = \frac{1}{Z}\sum_\alpha \langle\vec{R}|\alpha\rangle e^{-\beta E_\alpha} \tag{15}$$

with E_α the scattering energy, Z the partition function and $\beta = 1/(k_B T)$ with the Boltzmann constant k_B and the sample temperature T. The measured photoassociation probability thus corresponds to the thermal average

$$\langle P_{\nu,K}\rangle = \left|\langle\varphi_{n,L=0,0}|d^{(2)}|g\rangle\right|^2 \times \frac{1}{Z}\sum_\alpha |F_\alpha(0,0,N)|^2 e^{-\beta E_\alpha} . \tag{16}$$

In the limit that the rotational and vibrational motions are well separated, the pair correlation can be approximated [79] as

$$g^{(2)}\left(\vec{R}\right) \propto \sum_N \frac{1}{Z}\sum_\alpha |F_\alpha(0,0,N)|^2 e^{-\beta E_\alpha} \tag{17}$$

which can be extracted from the measured photoassociation probability. For principal quantum numbers $20 \lesssim n \lesssim 79$, R_n varies between ~25 and 500 nm, allowing correlations to be measured over this previously inaccessible length scale [34, 35] (see also [80, 81]).

Initial studies centered on the role of quantum statistics. For a gas in which the nuclear spin $\vec{I}$ is nearly aligned or gas of $I = 0$ atoms, the spin wavefunction of a two-body state is symmetric under the exchange of the two atoms. Therefore,

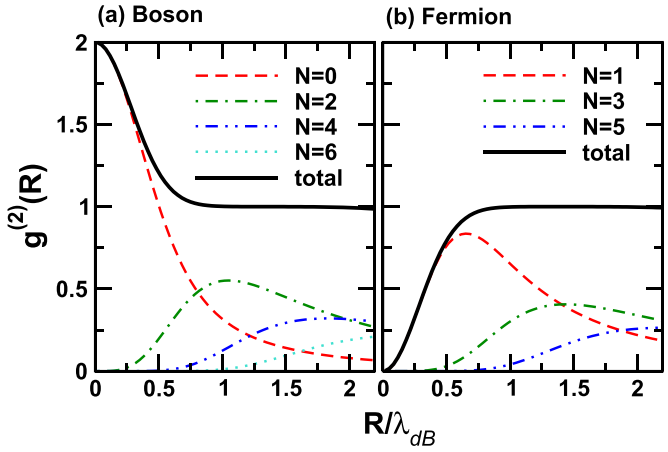

Figure 4. Values of $g^{(2)}(R)$ for ^{84}Sr and spin-polarized ^{87}Sr expressed as a function of $R/\lambda_{\rm dB}$ showing the contributions from the different rotational states. For bosons (fermions) only states with even (odd) values of N contribute to $g^{(2)}(R)$.

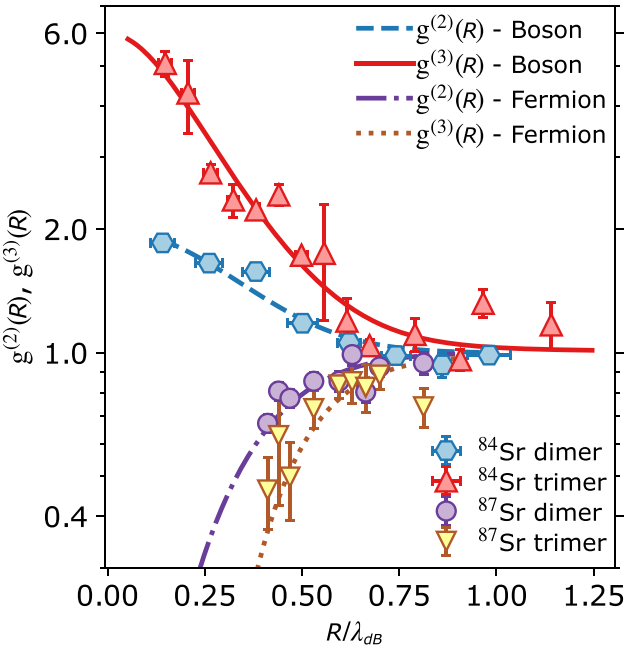

Figure 5. Measured and calculated values of $g^{(3)}(R)$ and $g^{(2)}(R)$ for ultracold gases of bosonic (^{84}Sr) and spin-polarized fermionic (^{87}Sr) atoms. R is taken to be the internuclear separation, R_n. (Reprinted figure with permission from [35], Copyright (2023) by the American Physical Society).

the rest of the wavefunction, i.e. the molecular orbital, has to be symmetric (even N) for bosons and anti-symmetric (odd N) for fermions to maintain the symmetry of the total wavefunction. In consequence, as shown in figure 4, in the limit that the internuclear separation R is much smaller than the de Broglie wavelength $\lambda_{\rm dB} = \sqrt{2\pi/(mk_{\rm B}T)}$, where s-wave scattering is dominant, scattering is suppressed for the fermions. However, as $R/\lambda_{\rm dB}$ increases, higher rotational states become important and provide major contributions to $g^{(2)}(R)$.

To explore the behavior of $g^{(2)}(R)$, non-degenerate gases of bosonic ^{84}Sr($I=0$) and fermionic ^{87}Sr($I=9/2$) atoms were prepared. For non-degenerate gases of non-interacting particles, $g^{(2)}(R)$ is given by

$$g^{(2)}(R) = 1 + \epsilon e^{-2\pi R^2/\lambda_{\rm dB}^2} \tag{18}$$

with $\epsilon = +1(-1)$ for bosons (spin-polarized fermions), and zero for classical systems [82] approximated by a gas of unpolarized ^{87}Sr. Therefore, the photoassociation probability for an unpolarized gas

$$\sum_N \langle P_{\nu=0,N}\rangle_{\rm unpol} \simeq |\langle \varphi_{n,L=0,0}|d^{(2)}|g\rangle|^2 \tag{19}$$

is interpreted as the two-photon transition strength. This can be used to extract the correlation function for a polarized gas, i.e.

$$g^{(2)}(R) \simeq \frac{\sum_N \langle P_{\nu=0,N}\rangle_{\rm pol}}{\sum_K \langle P_{\nu=0,N}\rangle_{\rm unpol}}. \tag{20}$$

The measured production rates for ^{84}Sr and spin-polarized ^{87}Sr gases, normalized against those seen with an unpolarized ^{87}Sr sample, are shown in figure 5 as a function of $R/\lambda_{\rm dB}$ measured at $R = R_n$. As $R/\lambda_{\rm dB}$ decreases, i.e. the sample temperatures decrease or n decreases, the increase in $g^{(2)}(R)$ due to bunching in the case of bosons is clearly evident, as is the decrease in $g^{(2)}(R)$ resulting from antibunching, i.e. Fermi repulsion, in the case of the (spin-polarized) fermions. The experimental results are in good agreement with theoretical predictions, i.e. equation (18). This protocol is also applicable for a gas of atoms that have a short range interaction as long as the interaction does not affect the formation of ULRMs.

Pair correlation studies were extended through measurements of the dimer formation rates for higher vibrational states whose wavefunctions span several wells in the molecular potential (see figure 3), which allows $g^{(2)}(R)$ to be probed at somewhat smaller length scales [79]. These studies further demonstrated the potential of ULRM formation as a probe of spatial correlations over intermediate length scales and provide a window into, for example, the formation of Halo states, [83], strongly-correlated one-dimensional gases [84, 85] and Efimov trimers [86].

Measurements have also been extended to trimer formation and the determination of higher-order spatial correlations [35]. A trimer ULRM contains two ground-state atoms, each in the vibrational ground state at a distance R_n from the core ion. Measurements of trimer formation can therefore be used to examine three-body spatial correlations. The relative angle, θ, between two ground state atoms is quantized through the mass polarization interaction but the resulting energy splitting is typically small ($\sim$100 kHz) [87] and challenging to resolve experimentally. Therefore, angle-averaged quantities are determined. The calculated θ-averaged values are presented in figure 5 together with the experimental

measurements which are again normalized against unpolarized ^{87}Sr measurements. For ^{84}Sr the trimer production rate increases dramatically with decreasing $R/\lambda_{\rm dB}$ but remains consistent with theoretical predictions, whereas for spin-polarized ^{87}Sr a marked reduction in the trimer production rate is seen, again consistent with theory. The results demonstrate just how much more sensitive trimer creation is to spatial correlations. Even higher-order correlations should be accessible by observing the formation of tetramers, and even higher p-mers, providing an opportunity for detailed characterization of correlations in many-body quantum systems. Indeed formation of a Rydberg polaron, a quasi-particle involving a Rydberg atom and ground-state atoms in the background gas, can be described by extending the theoretical model (equation (16)) of dimer formation to a many-body system allowing the density distribution of the initial ground-state atoms to be probed using the polaron excitation spectra. This will be discussed in more detail in section 8.

6. Rotational spectroscopy of ULRMs

Whereas the vibrational structure of dimer ULRMs was explored in some detail in early studies, it is only recently that it has become possible to explore their rotational structure [62], which provides another powerful probe of their properties [88]. The binding energy of the ground vibrational state of Sr ULRMs is on the order of 10 MHz for $n \sim 30$ while the centrifugal energy is much smaller, $\langle N^2\rangle/(2\mu R^2) \lesssim 100$ kHz. Typically, for temperatures of ~ 1 μK, where s-wave atom-atom scattering prevails, dimer production will lead principally to the formation of $N=0$ rotational states (i.e. the total angular momentum state $K=L$) whereupon the observation of rotationally-excited states will require both high resolution and good statistics to identify any small spectral features associated with their creation. Rotational structure can, however, be clearly seen when creating ^{86}Sr S-state dimers, facilitated by the large ^{86}Sr–^{86}Sr atom-atom s-wave scattering length, $a_s \sim 811 a_0$ (see table 1), which is comparable to the size of a Rydberg atom with $n \sim 25$. The s-wave component of the two-body scattering wavefunction $\langle \vec{R}|\alpha\rangle$ has a node at $R = a_s$. The Franck–Condon overlap with the ground vibrational state (equation (14)) is therefore reduced for Rydberg atoms with $R_n \sim a_s$, suppressing the s-wave channel and allowing the effects of higher partial wave scattering, which leads to the production of rotationally-excited states, to be observed. The approximation (equation (14)) for the Franck–Condon factor preserves the rotational quantum number N of the initial state $|\alpha\rangle$, which would suggest that only rotational states with even N would be created in a bosonic gas. However, the recoil momentum associated with photoexcitation of one of the initial atom pair to a Rydberg state can transfer angular momentum to the atom pair, which for a molecule with large bond length, can be sizable. An extended expression for the Franck–Condon factor becomes

$$F_\alpha(\nu, L, K) = \langle \nu, L, K|e^{i\vec{k}_L\cdot\vec{R}/2}|\alpha\rangle \qquad (21)$$

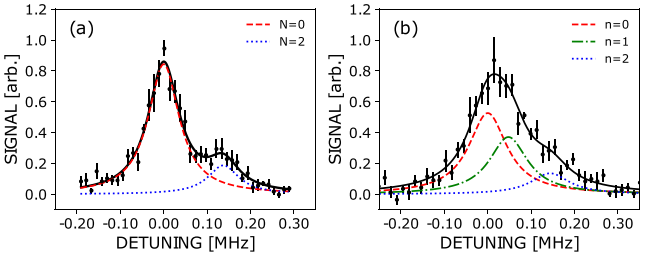

Figure 6. Measured photoexcitation spectra for creation of ^{86}Sr 29^1S_0 dimers in a cold gas using (a) counter- and, (b) co-propagating laser beams. (a) includes a two-component Lorentzian fit to the data, (b) a three-component fit to the data. Their separate contributions to the total dimer signal are also shown (see text). Adapted with permission from [89], copyright (2024) by the American Physical Society.

with the photon momentum $\vec{k}_L$. This form factor allows transitions between different rotational states and generation of odd-N rotational states.

Initial studies of rotational excitation focused on ^{86}Sr n^3S_1 dimers and demonstrated the production of rotationally-excited states with values of N as high as $N=3$ [88]. More recently, measurements have been extended to ^{86}Sr n^1S_0 dimers [89]. Such dimers offer the advantage that they can be created by two-photon excitation via the $5s5p$ $^1P_1$ intermediate state using lasers operating at 461 and 412 nm. Thus, if the laser beams counterpropagate, not only is the effective Doppler linewidth minimized, but so too is the net photon momentum transfer that accompanies Rydberg excitation, thereby providing a valuable benchmark against which to examine the effects of photon recoil momentum. The photoexcitation spectrum (figure 6(a)) recorded when creating $n=29$ $^1S_0$ dimers using counter-propagating laser beams can be well-fit by the sum of two Lorentzians whose separation matches that predicted using the Franck-Condon factor, equation (21), and is in good agreement with the expected difference in centrifugal energy $N(N+1)/(2\mu R_n^2)$ between the $N=0$ and $N=2$ rotational states. Using co-propagating laser beams (figure 6(b)) the spectrum can no longer be well fit by the sum of two contributions corresponding to the $N=0$ and $N=2$ levels. A three-component fit is required and demonstrates the presence of an additional feature whose separation from the $N=0$ state is consistent with the formation of $N=1$ rotationally-excited states, highlighting the important role that photon momentum transfer can play when creating rotationally-excited ULRMs. As n increases (above $n \sim 25$) the dimer internuclear separation R_n grows and suppression of the $N=0$ channel decreases. The total dimer signal increases and becomes dominated by $N=0$ production.

7. Heteronuclear ULRMs

Whereas the majority of studies of ULRMs to date have involved homonuclear dimers, trimers, and polyatomic ULRMs, several protocols have been proposed or

demonstrated to create their heteronuclear equivalents. Such species can now be studied in the laboratory with the advent of dual species traps that allow the generation of overlapping clouds of different atoms (and/or molecules).

Early studies of the formation of heteronuclear ULRMs in a two-component ultracold gas were theoretical and centered on the light alkali metal atoms [80]. Accurate electron-atom scattering phase shifts were first calculated and used in a spin-dependent theoretical model to calculate BO molecular potential curves for different alkali metal combinations. This work highlighted the variety of different molecular states that could be accessed through use of different alkali-metal combinations, including hybridized states that involve mixing of high-L trilobite states with isolated low-L states, facilitating their optical excitation. Also, this work showed that the different combinations possess markedly different spectroscopic signatures, allowing them to be readily distinguished from homonuclear molecules that might also be produced.

The first heteronuclear ULRMs created in the laboratory were generated in a mixture of ultracold ^{84}Sr and ^{88}Sr atoms held in the same optical dipole trap [90]. These dimers were created by excitation of minority ^{88}Sr atoms in a dense background of ^{84}Sr atoms and the product ^{84}Sr-^{88}Sr dimers identified through the isotope shifts in the $\nu = 0$ vibrational level. Essentially pure samples of ^{84}Sr-^{88}Sr dimers were produced, providing many new opportunities, for example, to measure inter-species correlation functions in multi-component many-body systems and the ^{84}Sr-^{88}Sr scattering wavefunction. Extension of measurements to heteronuclear trimers opens an opportunity to explore the sensitivity of the isotope shift to the mass polarization energy.

Heteronuclear ^{133}Cs-^{39}K long-range molecules have been created in a dual-species magneto-optical trap [91]. Millimeter-wave spectroscopy was used to probe molecular states correlating with different atomic angular momenta, and comparative measurements of KCs dimers were undertaken in which either the K or Cs atoms were excited to the Rydberg state.

The existence of a different type of polyatomic long-range Rydberg molecule comprising a Rydberg atom and polar molecule has also been proposed, with binding resulting from the interaction between the Rydberg electron and the permanent electric dipole moment of the trapped molecule [92]. By considering a nearly-degenerate set of high-L rubidium electronic states it was predicted that a Λ-doublet molecule (with a dipole moment, $d < 1.639$ D) can bind to a Rydberg atom. Calculations of the molecular BO potentials showed the product ULRMs to be relatively strongly bound, with binding energies of $\sim 10 - 20$ GHz, and possess very large electric dipole moments, $\gtrsim 1$ kD. Furthermore, they revealed two different sets of potential curves depending on whether the molecular dipole moment was oriented towards, or away from, the Rydberg core ion, resulting in two spatially and energetically separated sets of states. In subsequent work, theoretical calculations were extended to include coupling between the nS levels and nearby degenerate high-L manifolds [93]. Attention then focused on the Rb-KRb system and the effects of weak externally-applied electric fields [94]. Such fields distort the Rydberg electron wavefunction and hence the electric field experienced by the KRb molecule due to the Rydberg electron. This enables tuning of the molecular BO potentials and the introduction of s-wave character into the Rydberg wave function, facilitating their optical excitation. This work was extended to include the angular degrees of freedom of the molecule and its effects on molecular alignment and orientation [95]. Another possible protocol to form long-range K-KRb or Rb-KRb molecules in the laboratory was also considered that leveraged the rotational structure in the ground vibrational state of the KRb molecules to find advantageous admixtures of s or d Rydberg orbitals [96].

Recently it has also been predicted that ultralong-range Rydberg bi-molecules can be formed from a long-lived NO(nf, ng) Rydberg molecule and a (Λ-doublet) ground-state NO molecule. The calculated BO molecular potentials for NO($40f, 40g$)-NO($X^2\Pi_{1/2}$) molecules support deep vibrational levels with binding energies of ~0.5–1 GHz and kilodebye permanent electric dipole moments [97].

8. BECs and polaron physics

Ultracold gases play an important role in studies of many-body physics including the investigation of 'impurity' particles immersed in a complex many-body environment, the 'bath.' One such example is the dressing of the conduction electrons in a dielectric medium by collective excitations in the medium, i.e. phonons, which leads to formation of quasiparticles termed polarons [98]. Other areas where polarons are important include spin-current transport in organic semiconductors [99] and optical absorption of two-dimensional materials [100, 101].

In initial studies of polaron physics in cold gases [102], polarons were realized using a population-imbalanced atomic gas, the minority atoms playing the role of the 'impurity,' the majority atoms the role of the 'bath', i.e. medium. Studies conducted using both bosonic and fermionic baths showed that the properties of the system depend strongly on the quantum nature of the bath [103–107].

More recently, studies of polaron physics have been extended to include so-called Rydberg polarons created by excitation of high-n Rydberg atoms as impurities in a dense strontium Bose–Einstein condensate (BEC) under conditions where the Rydberg electron orbit encloses tens to hundreds of ground-state atoms [36, 37]. Rydberg polarons provide a new window into polaron physics because, unlike polarons seen in condensed matter physics, their creation is accompanied by macroscopic occupation of bound molecular states. This is illustrated in the inset in figure 7. Laser excitation creates an 'impurity', the Rydberg atom, in the BEC resulting in a mix of final states that includes both scattering states and bound molecular states. This mix can be probed experimentally through spectroscopy. Although Rydberg atom experiments in rubidium BECs were carried out earlier [50, 64], the presence of the p-wave shape resonance complicates any identification of polaron features.

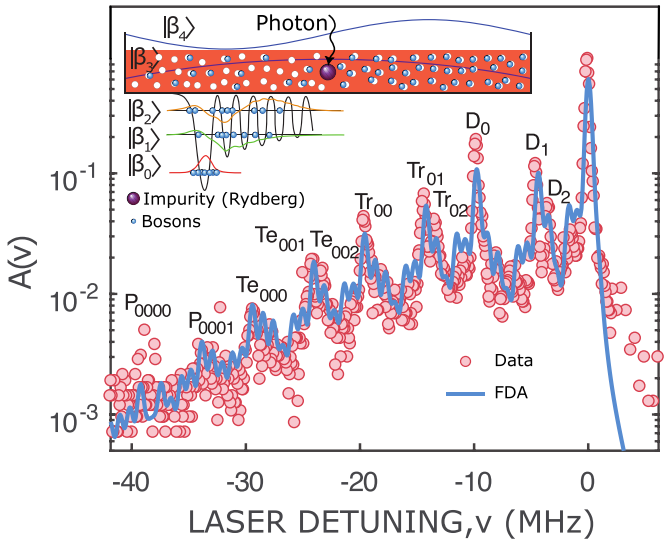

Figure 7. Spectrum for photoexcitation of $5s38s\ ^3S_1$ ULRMs in an ^{84}Sr BEC in the few-body regime. The ground and vibrationally-excited molecular states are labeled (D-dimer, Tr-trimer, Te-tetramer, and P-pentamer). The figure includes the FDA predictions. The inset shows a schematic of the creation of a Rydberg polaron in a uniform density BEC. Laser excitation projects the system into a mix of final configurations comprising atoms in both bound and scattering states, $|\beta_i\rangle$. (Reprinted figure with permission from [36], Copyright (2018) by the American Physical Society).

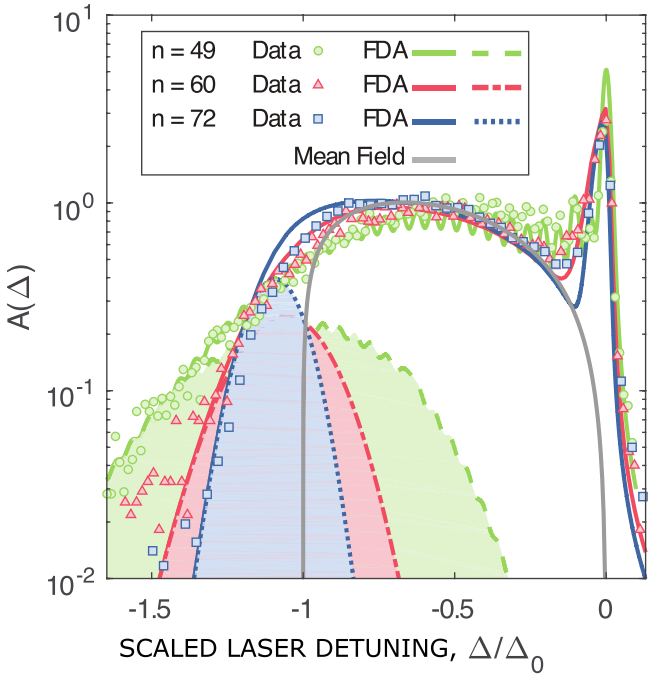

Figure 8. Spectrum for excitation of states with $n = 49$, 60, and 72 in the many-body regime (see text). The laser detuning is normalized to the red cut-off of the predicted mean-field spectrum. The shaded regions represent the FDA predicted polaron response from the center of the atom cloud demonstrating that polaron formation can account for the tail in the distribution (see text). (Reprinted figure with permission from [36], Copyright (2018) by the American Physical Society).

The Rydberg polaron can be described by the Hamiltonian

$$H = \frac{P_0^2}{2m} + \sum_i \frac{P_i^2}{2\mu} + V_M(R_i)\ . \tag{22}$$

$\vec{P}_0$ is the momentum of the mobile impurity (Rydberg atom), $\vec{R}_i$ and $\vec{P}_i$ are the position and momentum of the (bosonic) ground-state atoms, and $V_M(R)$ is the interaction between a ground-state atom and the Rydberg atom (equation (4)). The interaction between bosons and the mass polarization interaction are typically small and neglected. Using the Bogoliubov approximation the Hamiltonian can be transformed to the the widely-used Fröhlich Hamiltonian, which is the basis for various polaron models [37] and the polaron excitation dynamics analyzed using a functional determinant approach (FDA). In this approach [38] polaron excitation is treated using an analogous approach to that used for Rydberg dimer formation (section 5) by replacing the Franck–Condon factor (equation (14)) with the overlap between a many-body scattering state and a Rydberg polaron. In the limit of only weak interactions between ground-state atoms the Franck-Condon factor for a polaron can be factorized to a product of the two-body Franck-Condon factors (equation (14)) assuming that each ground-state atom occupies an unperturbed dimer level (both bound and unbound). Within the local density approximation, the initial scattering wavefunction is assumed to be constant and normalized to the local density near the impurity. The eigenenergy of the Rydberg polaron can be estimated from the local density and distribution of dimer levels.

Figure 7 shows the spectrum for excitation of Sr$(5s38s)^3S_1$ atoms in a BEC in the few-body regime where, on average, three ground-state atoms are present within the Rydberg electron cloud. Multiple individual spectral lines are evident that result from the creation of Rydberg dimers, trimers,... in ground and vibrationally-excited states. The theoretical FDA prediction is in remarkable agreement with experiment over several orders of magnitude.

For higher n where the Rydberg atom encloses tens to hundreds of ground-state atoms and many-body effects become important, the spectrum evolves into a broad continuum (figure 8). To identify the effects of polaron excitation, figure 8 includes the results of a mean-field treatment, in which each ground state atom is assumed to induce the same energy shift given by the mean interaction $\langle V_M \rangle$ and the total energy shift is determined solely by the local density of atoms within the BEC [37]. Whereas the mean-field theory matches well the spectrum at intermediate detunings, it fails to reproduce the resolved few-body features observed at small detunings and the red-detuned tail. FDA allows the contribution to the overall spectrum from the high-density central portion of the BEC to be isolated and, as shown by the shaded regions in figure 8 accounts for the tail. Several important questions remain, such as the extent to which notions of effective mass, mobility, and polaron-polaron interactions are applicable to Rydberg polarons, and whether interactions are sufficient to

lead to self-localization of the impurity. Rydberg excitations in high-density media have also been discussed using quasi-static lineshape theory [39].

More recent calculations have explored the absorption spectrum of a Rydberg atom excited in a structured environment, i.e. lattice [108, 109], and in an ideal BEC [110], together with the changes that occur as the local density is increased. For a BEC, at low densities a positive-energy spectral feature is seen which is identified as a repulsive polaron as well as a series of negative energy peaks, i.e. attractive polarons, that are associated with molecular bound states that can be occupied to form dimers, trimers, $\cdots$. These are, however, dressed by bath excitations and therefore each ULRM possesses some quasi-particle character inherited from the repulsive polaron and forms a "molaron" with a binding energy shifted from that of the bare dimer, trimer $\cdots$. This small many-body shift, however, has yet to be observed experimentally. As the density increases, the spectral weight shifts entirely into molaron states. Their absorption peaks blend together and a universal Gaussian response emerges as the statistical nature of the bath comes to dominate its quantum dynamics. Although the shifts associated with the formation of repulsive polarons are small, given the improved laser resolution now available it should be possible to detect their formation experimentally [110].

Following excitation of a single atom in a BEC to a highly-excited Rydberg state, scattering of the Rydberg electron sets the ground-state atoms within the electron cloud into motion, thereby opening up the opportunity to study the many-body dynamics of atoms moving within an atom [111–114]. Such dynamics have been examined theoretically through simulations that consider both single and multiple excitations within a BEC. The simulations, which consider different interaction potentials and levels of approximation, address not only the fast dynamics associated with the small-scale radial modulations in the (Rydberg) molecular potential (see figure 3) but also the slower dynamics due to the classically-averaged potential that result in density waves that, at late times, emerge outside the Rydberg excitation volume. The simulations suggest that BECs can form a valuable platform for *in situ* and real time examination of ultra-cold chemical dynamics involving Rydberg states.

Interestingly, it has also been proposed to take advantage of the nearly constant bond-length in ground-state ($\nu = 0$) ULRM dimers to enable *in situ* spectroscopic imaging of the polaron cloud in an ultracold Fermi gas [115]. The ULRM bond length, R_n, can be tuned through the polaron cloud, thereby forming a precision sensor inserted into the cloud. This approach also promises to allow studies of polaron formation in real time and to investigate polarons created in a BCS superfluid [116, 117]. This differs from probing a BEC using Rydberg impurities because, for fermionic systems, the number of particles within the Rydberg radius remains small.

BECs combined with ULRM creation also provide an opportunity to study molecular behavior in a quantum solvent (the BEC) [118]. This was demonstrated through experiments in which alkali S and D state dimers were first created in a BEC and which then underwent internal conversion to a trilobite state (in which the Rydberg electron is maximally localized). The energy released is distributed within the medium, accelerating condensate atoms resulting in a decrease in the local BEC density that is detected through optical microscopy. This platform promises to allow the direct study of exotic quantum chemical reactions in a quantum degenerate solvent.

9. Lifetime of Rydberg molecules (polarons)

Excitation of a Rydberg atom in an ultracold gas of atoms leads to a formation of Rydberg polarons. The influence of scattering states increases with the density of atoms and the effect of collisions can be observed through their effect on the ULRM lifetime.

The first measurements of ULRM lifetimes were undertaken using Rb $^3\Sigma(ns - 5s)$ dimers with $34 \leqslant n \leqslant 43$ and relatively low trap densities, $\sim 10^{13}$ cm^{-3}, corresponding to < 0.1 ground-state atoms within the Rydberg electron orbit. The molecular lifetimes were observed to be substantially smaller than those of the parent Rydberg atoms and the lifetime of the first excited vibrational state was seen to be less than that of the ground vibrational state [119], which was attributed to the atom pair being able to penetrate to smaller separations in the excited vibrational state. Comparison to classical scattering theory suggested that the reduced lifetime could be explained as a perturbation of the molecular state by the surrounding ground-state atoms.

In a subsequent series of rubidium experiments [50] at higher n, $50 < n < 150$, and higher trap densities, $\sim 1 - 5 \times 10^{14}$ cm^{-3}, there were, on average, up to a few thousand ground-state atoms contained within the Rydberg cloud, allowing creation of polyatomic Rydberg molecules and Rydberg polarons [114]. The high density facilitates collisions between the Rydberg ion core and ground-state atoms for which, at low temperatures, the associated Langevin cross section [120, 121] becomes comparable to the size of the Rydberg molecule. The measured lifetimes ranged from less than 1 μs ($n \sim 50$) to ~10 μs ($n > 100$), much shorter than those observed in low density samples.

Two different loss channels were identified, both of which involved a close encounter between the Rydberg core ion and a ground-state atom. For rubidium, avoided crossings between the BO potential surfaces are formed due to the p-wave shape resonance (figure 2). As the ground state atom approaches the ion core, the Rydberg electron can be transferred to a butterfly state via an avoided crossing and, eventually, to a lower-lying different L level. In this L-changing process, the energy released is shared by the ion-atom pair leading to dissociation, the Rydberg electron remaining attached to the core ion but in a different Rydberg state. Measurement of the velocity distribution of the product Rydberg atoms showed the energy transfer to be associated with a transition from the initial nS level to the lower-lying neighboring $(n-4)$ hydrogenic manifold. Further evidence of such L-changing was

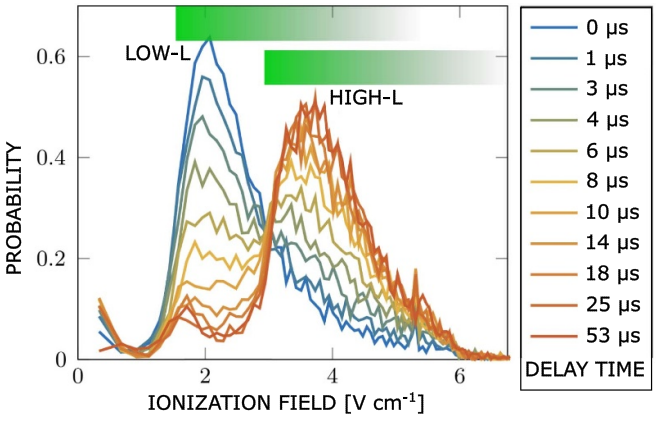

Figure 9. Time development of the SFI spectrum following formation of high-n, $n = 121$, dimers. At early times, when dimers dominate the spectrum, the ionization signal results from ionization of low-L states. At late times where much of the signal results from ionization of Rydberg atoms that result from dissociation, high-L states dominate. The bars indicate the ranges of applied field over which the high- and low-L states are expected to ionize. (Reprinted figure with permission from [50], Copyright (2016) by the American Physical Society).

provided by monitoring changes in the Rydberg atom population distribution using selective field ionization (SFI). The transition from initial low-L states to high-L final product states is clearly seen in the evolution of the SFI spectrum as shown in figure 9. (For a more detailed discussion of state-changing in collisions between Rydberg atoms and ground-state atoms, see, for example, [122])

The second loss channel identified was associative ionization. As a ground-state atom approaches the core ion it is accelerated by the short-range attractive interaction between the ion and the atom,

$$V_{\rm pol}(R) = -\frac{\alpha}{2R^4}, \tag{23}$$

with α the polarizability of the ground-state atom. This opens a possibility to form a molecular ion Rb_2^+ through associative ionization,

$$Rb^* + Rb \rightarrow Rb_2^+ + e^- \tag{24}$$

during a close ion-ground state atom encounter, with the Rydberg electron carrying off the excess energy. The product Rb_2^+ ions were observed directly through measurements of ion flight times.

Lifetime studies using strontium dimers revealed rather different behavior to that seen with rubidium. In particular, measurements using strontium n^3S_1 dimers and relatively low trap densities [123] showed that the lifetimes of dimers in the low-lying vibrational states ($\nu = 0, 1$) were very similar to those of the parent atoms and only slightly shorter for $\nu = 2$ states, pointing to a very small probability for the dimer ground-state atom to approach close to the core ion. This contrasts with the behavior seen for rubidium and can be attributed to the very different potential energy landscapes. For strontium there is no p-wave 'butterfly' state, transitions to which can accelerate the core ion towards the ground-state atom thereby enhancing the collision rate.

Strontium lifetime measurements were also extended to higher n, $50 \lesssim n \lesssim 150$, and dense atomic samples, $\sim 1 - 3 \times 10^{14}$ cm^{-3}, contained in a BEC [124, 125]. The Rydberg lifetimes, $\sim 2 - 10\,\mu$s, were found to be very much less than those of the parent Rydberg atoms. However, for the lower values of n, $n \lesssim 100$, the measured lifetimes were again significantly longer than those seen for rubidium. For strontium the observed loss rates were consistent with a reaction model that emphasized the interaction between the core ion and nearest-neighbor ground-state atom. However, when the average collision rate was calculated it was found that the reaction rates were smaller than the predicted binary collision rate, suggesting that multiple core-ion-ground-state-atom collisions may be required before reaction occurs.

10. Outlook

ULRMs play an important role in the study of cold quantum gases and provide a valuable window into, for example, low-energy electron scattering, the role of quantum statistics in governing particle distributions, and into few- and many-body physics in general.

Continuing developments in theory including, for example, the inclusion of spin-orbit effects and the use of new approaches, promise ever more accurate and detailed predictions of ULRM vibrational and rotational structure. Improvements in experimental technique, such as the use of microwave spectroscopy to provide more accurate measurements of ULRM rovibrational structure, will provide a more stringent test of theory and, in turn, an improved understanding of low-energy electron-atom (and molecule) scattering.

The large number of atomic species that have been, or potentially can be, laser cooled and trapped (see, for example [81, 126–128]), will enable studies of ULRM formation using a range of Rydberg atoms with very different electronic (and core ion) structures. Advances in the production of overlapping clouds of cold atoms will facilitate further studies of heterogeneous ULRMs. The creation of cold molecular gases will allow studies of ULRMs that involve not only trapped molecules but also ULRMs based on molecular Rydberg states [97]. This flexibility will enable production of ULRMs with properties tailored to meet a variety of different needs or applications. Such measurements promise new insights into electron-molecule scattering and into the myriad processes that can occur through energy interchange between the Rydberg electron and internal motions within the molecule.

ULRM formation will continue to provide an important tool with which to study non-local pair (and higher-order) correlations in ultracold gases, i.e. quantum fluids. Studies with BECs can illuminate the emergence of collective behaviors such as the creation of Rydberg polarons. ULRM formation also provides a valuable diagnostic for probing atoms held in optical lattices [129] or tweezers [130] enabling, for example,

identification of site double occupancy [81] or, if the intersite spacing is sufficiently small, the occupancy of neighboring sites. For a strongly interacting Bose gas with very tight radial confinement held in a two-dimensional lattice, a reduction in ULRM formation might signal the emergence of particle correlations that match those of a gas of fermions and creation of a Tonks gas [85, 131].

Data availability statement

All data that support the findings of this study are included within the article (and any supplementary files).

Acknowledgments

The authors acknowledge valuable discussions with their colleagues, T C Killian, Y Lu, and C Wang during preparation of this review. Their research was supported by the NSF under Grant No. 1904294, and the AFOSR FA9550-17-1-0366. The authors acknowledge TU Wien Bibliothek for financial support through its Open Access Funding Program.

ORCID iDs

F B Dunning https://orcid.org/0000-0003-3368-0519
S K Kanungo https://orcid.org/0000-0002-6182-8827
S Yoshida https://orcid.org/0000-0002-6649-7692

References

[1] Greene C H, Dickinson A S and Sadeghpour H R 2000 Creation of polar and nonpolar ultra-long-range Rydberg molecules *Phys. Rev. Lett.* **85** 2458–61
[2] Bendkowsky V, Butscher B, Nipper J, Shaffer J P, Löw R and Pfau T 2009 Observation of ultralong-range Rydberg molecules *Nature* **458** 1005
[3] Shaffer J P, Rittenhouse S T and Sadeghpour H R 2018 Ultracold Rydberg molecules *Nat. Commun.* **9** 1965
[4] Fey C, Hummel F and Schmelcher P 2020 Ultralong-range Rydberg molecules *Mol. Phys.* **118** e1679401
[5] Saßmannshausen H, Deiglmayr J and Merkt F 2016 Long-range Rydberg molecules, Rydberg macrodimers and Rydberg aggregates in an ultracold Cs gas *Eur. Phys. J. Spec. Top.* **225** 2891
[6] Lippe C, Eichert T, Thomas O, Niederprüm T and Ott H 2019 Excitation of Rydberg molecules in ultracold quantum gases *Phys. Status Solidi* b **256** 1800654
[7] Eiles M T 2019 Trilobites, butterflies and other exotic specimens of long-range Rydberg molecules *J. Phys. B: At. Mol. Opt. Phys.* **52** 113001
[8] Sadeghpour H R 2023 Ultracold Rydberg atom-atom interactions *Springer Handbook of Atomic, Molecular and Optical Physics* vol 63, ed G W F Drake (Springer) pp 795–802
[9] Merkt F 1997 Molecules in high Rydberg states *Annu. Rev. Phys. Chem.* **48** 675
[10] Reinhold E and Ubachs W 2005 Heavy Rydberg states *Mol. Phys.* **103** 1329
[11] Reinhold C O, Yoshida S and Dunning F B 2011 Electric-field-induced dissociation of heavy Rydberg ion-pair states *J. Chem. Phys.* **134** 174305
[12] Vieitez M O, Ivanov T I, Reinhold E, de Lange C A and Ubachs W 2008 Observation of a Rydberg series in H^+H^-: a heavy Bohr atom *Phys. Rev. Lett.* **101** 163001
[13] Mollet S and Merkt F 2010 Dissociation dynamics of ion-pair states of Cl_2 at principal quantum numbers beyond 1500 *Phys. Rev.* A **82** 032510
[14] Beyer M and Merkt F 2018 Communication: heavy-Rydberg states of HD and the electron affinity of the deuterium atom *J. Chem. Phys.* **149** 031102
[15] Dunning F B and Buathong S 2018 Collisions of Rydberg atoms with neutral targets *Int. Rev. Phys. Chem.* **37** 287–328
[16] Cannon M, Wang C H, Dunning F B and Reinhold C O 2010 Lifetimes of heavy-Rydberg ion-pair states formed through Rydberg electron transfer *J. Chem. Phys.* **133** 064301
[17] Hummel F, Schmelcher P, Ott H and Sadedhpour H R 2020 An ultracold heavy Rydberg system formed from ultra-long-range molecules bound in a stairwell potential *New J. Phys.* **22** 063060
[18] Peper J M and Deiglmayr J 2020 Formation of ultracold ion pairs through long-range Rydberg molecules *J. Phys. B: At. Mol. Opt. Phys.* **53** 064001
[19] Hollerith S and Zeiher J 2023 Rydberg macrodimers: Diatomic molecules on the micrometer scale *J. Phys. Chem.* A **127** 3925
[20] Weber S, Tresp C, Menke H, Urvoy A, Firstenberg O, Büchler H P and Hofferberth S 2017 Calculation of Rydberg interaction potentials *J. Phys. B: At. Mol. Opt. Phys.* **50** 133001
[21] Overstreet K R, Schwettmann A, Tallant J, Booth D and Shaffer J P 2009 Observation of electric-field-induced Cs Rydberg atom macrodimers *Nat. Phys.* **5** 581
[22] Saßmannshausen H and Deiglmayr J 2016 Observation of Rydberg-atom macrodimers: Micrometer-sized diatomic molecules *Phys. Rev. Lett.* **117** 083401
[23] Hollerith S, Zeiher J, Rui J, Rubio-Abadal A, Walther V, Pohl T, Stamper-Kurn D M, Bloch I and Gross C 2019 Quantum gas microscopy of Rydberg macrodimers *Science* **364** 664
[24] Duspayev A, Han X, Viray M A, Ma L, Zhao J and Raithel G 2021 Long-range Rydberg-atom–ion molecules of Rb and Cs *Phys. Rev. Res.* **3** 023114
[25] Deiß M, Haze S and Hecker Denschlag J 2021 Long-range atom-ion Rydberg molecule: a novel molecular binding mechanism *Atoms* **9** 34
[26] Zuber N, Anasuri V S V, Berngruber M, Zou Y-Q, Meinert F, Löw R and Pfau T 2022 Observation of a molecular bond between ions and Rydberg atoms *Nature* **605** 453
[27] Zou Y-Q, Berngruber M, Anasuri V S V, Zuber N, Meinert F, Löw R and Pfau T 2023 Observation of vibrational dynamics of orientated Rydberg-atom-ion molecules *Phys. Rev. Lett.* **130** 023002
[28] R F Stebbings and F B Dunning ed 1983 *Rydberg States of Atoms and Molecules*, (Cambridge University Press)
[29] Gallagher T F 1994 *Rydberg Atoms* (Cambridge University Press)
[30] Jeys T H, Foltz G W, Smith K A, Beiting E J, Kellert F G, Dunning F B and Stebbings R F 1980 Diabatic field ionization of highly excited sodium atoms *Phys. Rev. Lett.* **44** 390–3
[31] Gallagher T F, Humphrey L M, Hill R M and Edelstein S A 1976 Resolution of $|m_l|$ and $|m_j|$ levels in the electric field ionization of highly excited *d* states of Na *Phys. Rev. Lett.* **37** 1465–7
[32] Schlagmüller M *et al* 2016 Probing an electron scattering resonance using Rydberg molecules within a dense and ultracold gas *Phys. Rev. Lett.* **116** 053001

[33] Engel F, Dieterle T, Hummel F, Fey C, Schmelcher P, Löw R, Pfau T and Meinert F 2019 Precision spectroscopy of negative-ion resonances in ultralong-range Rydberg molecules *Phys. Rev. Lett.* **123** 073003

[34] Whalen J D, Kanungo S K, Ding R, Wagner M, Schmidt R, Sadeghpour H R, Yoshida S, Burgdörfer J, Dunning F B and Killian T C 2019 Probing nonlocal spatial correlations in quantum gases with ultra-long-range Rydberg molecules *Phys. Rev.* A **100** 011402

[35] Kanungo S K, Lu Y, Dunning F B, Yoshida S, Burgdörfer J and Killian T C 2023 Measuring nonlocal three-body spatial correlations with Rydberg trimers in ultracold quantum gases *Phys. Rev.* A **107** 033322

[36] Camargo F *et al* 2018 Creation of Rydberg polarons in a Bose gas *Phys. Rev. Lett.* **120** 083401

[37] Schmidt R *et al* 2018 Theory of excitation of Rydberg polarons in an atomic quantum gas *Phys. Rev.* A **97** 022707

[38] Tempere J, Casteels W, Oberthaler M K, Knoop S, Timmermans E and Devreese J T 2009 Feynman path-integral treatment of the BEC-impurity polaron *Phys. Rev.* B **80** 184504

[39] Scheuing T and Pérez-Ríos J 2023 Quasi-static lineshape theory for Rydberg excitations in high-density media *Atoms* **11** 6

[40] Amaldi E and Segrè E 1934 Effetto della pressione sui termini elevati degli alcalini *Il Nuovo Cimento* **11** 145

[41] Amaldi E and Segrè E 1934 Effect of pressure on high terms of alkaline spectra *Nature* **133** 141

[42] Füchtbauer C and Gössler F 1934 Verschiebung und unsymmetrische verbreiterung von absorptionslinien durch fremdgase *Z. Phys.* **87** 89

[43] Fermi E 1934 Sopra lo spostamento per pressione delle righe elevate delle serie spettrali *Il Nuovo Cimento* **11** 157

[44] Omont A 1977 On the theory of collisions of atoms in Rydberg states with neutral particles *J. Phys.* **38** 1343

[45] Liebisch T C *et al* 2016 Controlling Rydberg atom excitations in dense background gases *J. Phys. B: At. Mol. Opt. Phys.* **49** 182001

[46] Munkes F *et al* 2024 Collisional shift and broadening of Rydberg states in nitric oxide at room temperature *Phys. Rev.* A **109** 032809

[47] Granger B E, Hamilton E L and Greene C H 2001 Quantum and semiclassical analysis of long-range Rydberg molecules *Phys. Rev.* A **64** 042508

[48] Li W *et al* 2011 A homonuclear molecule with a permanent electric dipole moment *Science* **334** 1110–4

[49] Hamilton E L, Greene C H and Sadeghpour H R 2002 Shape-resonance-induced long-range molecular Rydberg states *J. Phys. B: At. Mol. Opt. Phys.* **35** L199

[50] Schlagmüller M *et al* 2016 Ultracold chemical reactions of a single Rydberg atom in a dense gas *Phys. Rev.* X **6** 031020

[51] Hummel F, Schmelcher P and Eiles M T 2023 Vibronic interactions in trilobite and butterfly Rydberg molecules *Phys. Rev. Res.* **5** 013114

[52] DeSalvo B J, Aman J A, Dunning F B, Killian T C, Sadeghpour H R, Yoshida S and Burgdörfer J 2015 Ultra-long-range Rydberg molecules in a divalent atomic system *Phys. Rev.* A **92** 031403

[53] Bartschat K and Sadeghpour H R 2002 Ultralow-energy electron scattering from alkaline-earth atoms: the scattering-length limit *J. Phys. B: At. Mol. Opt. Phys.* **36** L9

[54] Eiles M T and Greene C H 2015 Ultracold long-range Rydberg molecules with complex multichannel spectra *Phys. Rev. Lett.* **115** 193201

[55] Fey C, Kurz M, Schmelcher P, Rittenhouse S T and Sadeghpour H R 2015 A comparative analysis of binding in ultralong-range Rydberg molecules *New J. Phys.* **17** 055010

[56] Seaton M J 1983 Quantum defect theory *Rep. Prog. Phys.* **46** 167

[57] Tarana M 2020 Long-range Rydberg molecule Rb_2: two-electron R-matrix calculations at intermediate internuclear distances *Phys. Rev.* A **102** 062802

[58] Giannakeas P, Eiles M T, Robicheaux F and Jan M R 2020 Generalized local frame-transformation theory for ultralong-range Rydberg molecules *Phys. Rev.* A **102** 033315

[59] Greene C H and Eiles M T 2023 Green's-function treatment of Rydberg molecules with spins *Phys. Rev.* A **108** 042805

[60] Srikumar R, Hummel F and Schmelcher P 2023 Nonadiabatic interaction effects in the spectra of ultralong-range Rydberg molecules *Phys. Rev.* A **108** 012809

[61] Bransden B H and Joachain C J 2003 *Physics of Atoms and Molecules* 2nd ed (Prentice-Hall)

[62] Thomas O, Lippe C, Eichert T and Ott H 2018 Photoassociation of rotating ultra-long range Rydberg molecules *J. Phys. B: At. Mol. Opt. Phys.* **51** 155201

[63] Bendkowsky V *et al* 2010 Rydberg trimers and excited dimers bound by internal quantum reflection *Phys. Rev. Lett.* **105** 163201

[64] Gaj A, Krupp A T, Balewski J B, Löw R, Hofferberth S and Pfau T 2014 From molecular spectra to a density shift in dense Rydberg gases *Nat. Commun.* **5** 4546

[65] Bellos M A, Carollo R, Banerjee J, Eyler E E, Gould P L and Stwalley W C 2013 Excitation of weakly bound molecules to trilobitelike Rydberg states *Phys. Rev. Lett.* **111** 053001

[66] Saßmannshausen H, Merkt F and Deiglmayr J 2015 Experimental characterization of singlet scattering channels in long-range Rydberg molecules *Phys. Rev. Lett.* **114** 133201

[67] Krupp A T, Gaj A, Balewski J B, Ilzhöfer P, Hofferberth S, Löw R, Pfau T, Kurz M and Schmelcher P 2014 Alignment of *D*-state Rydberg molecules *Phys. Rev. Lett.* **112** 143008

[68] Anderson D A, Miller S A and Raithel G 2014 Photoassociation of long-range *nD* Rydberg molecules *Phys. Rev. Lett.* **112** 163201

[69] Booth D, Rittenhouse S T, Yang J, Sadeghpour H R and Shaffer J P 2015 Production of trilobite Rydberg molecule dimers with kilo-Debye permanent electric dipole moments *Science* **348** 99

[70] Althön M, Exner M, Blättner R and Ott H 2023 Exploring the vibrational series of pure trilobite Rydberg molecules *Nat. Commun.* **14** 8108

[71] Niederprüm T, Thomas O, Eichert T, Lippe C, Pérez-Ríos J, Greene C H and Ott H 2016 Observation of pendular butterfly Rydberg molecules *Nat. Commun.* **7** 12820

[72] McQuillen P, Zhang X, Strickler T, Dunning F B and Killian T C 2013 Imaging the evolution of an ultracold strontium Rydberg gas *Phys. Rev.* A **87** 013407

[73] Brienza R, Fields G and Dunning F B 2021 Use of autoionization to measure microwave-driven transitions between high-*n* strontium Rydberg states *Rev. Sci. Inst.* **92** 075105

[74] Stellmer S, Grimm R and Schreck F 2013 Production of quantum-degenerate strontium gases *Phys. Rev.* A **87** 013611

[75] Bahrim C and Thumm U 2000 Low-lying $^3P^o$ and $^3S^e$ states of Rb^-,Cs^- and Fr^- *Phys. Rev.* A **61** 022722

[76] Deiß M, Haze S, Wolf J, Wang L, Meinert F, Fey C, Hummel F, Schmelcher P and Hecker Denschlag J 2020 Observation of spin-orbit-dependent electron scattering using long-range Rydberg molecules *Phys. Rev. Res.* **2** 013047

[77] Giannakeas P, Eiles M T, Robicheaux F and Rost J M 2020 Dressed ion-pair states of an ultralong-range Rydberg molecule *Phys. Rev. Lett.* **125** 123401

[78] Bai S, Han X, Bai J, Jiao Y, Zhao J, Jia S and Raithel G 2020 Cesium $nD_J + 6S1/2$ Rydberg molecules and their permanent electric dipole moments *Phys. Rev. Res.* **2** 033525

[79] Ding R, Kanungo S K, Whalen J D, Killian T C, Dunning F B, Yoshida S and Burgdorfer J 2020 Creation of vibrationally-excited ultralong-range Rydberg molecules in polarized and unpolarized cold gases of ^{87}Sr *J. Phys. B: At. Mol. Opt. Phys.* **53** 014002

[80] Eiles M T 2018 Formation of long-range Rydberg molecules in two-component ultracold gases *Phys. Rev.* A **98** 042706

[81] Manthey T, Niederprüm T, Thomas O and Ott H 2015 Dynamically probing ultracold lattice gases via Rydberg molecules *New J. Phys.* **17** 103024

[82] Naraschewski M and Glauber R J 1999 Spatial coherence and density correlations of trapped Bose gases *Phys. Rev.* A **59** 4595–607

[83] Köhler T, Góral K and Julienne P S 2006 Production of cold molecules via magnetically tunable Feshbach resonances *Rev. Mod. Phys.* **78** 1311–61

[84] Laburthe Tolra B, O'Hara K M, Huckans J H, Phillips W D, Rolston S L and Porto J V 2004 Observation of reduced three-body recombination in a correlated 1D degenerate Bose gas *Phys. Rev. Lett.* **92** 190401

[85] Kinoshita T, Wenger T and Weiss D S 2004 Observation of a one-dimensional Tonks-Girardeau gas *Science* **305** 1125

[86] Chin C, Grimm R, Julienne P and Tiesinga E 2010 Feshbach resonances in ultracold gases *Rev. Mod. Phys.* **82** 1225–86

[87] Fey C, Kurz M and Schmelcher P 2016 Stretching and bending dynamics in triatomic ultralong-range Rydberg molecules *Phys. Rev.* A **94** 012516

[88] Lu Y, Whalen J D, Kanungo S K, Killian T C, Dunning F B, Yoshida S and Burgdörfer J 2022 Resolving rotationally excited states of ultralong-range Rydberg molecules *Phys. Rev.* A **106** 022809

[89] Wang C, Lu Y, Kanungo S K, Dunning F B, Killian T C and Yoshida S 2024 Elucidating the roles of collision energy and photon momentum transfer in the formation of ultralong-range Rydberg molecules *Phys. Rev.* A **110** 032803

[90] Whalen J D, Kanungo S K, Lu Y, Yoshida S, Burgdörfer J, Dunning F B and Killian T C 2020 Heteronuclear Rydberg molecules *Phys. Rev.* A **101** 060701

[91] Peper M and Deiglmayr J 2021 Heteronuclear long-range Rydberg molecules *Phys. Rev. Lett.* **126** 013001

[92] Rittenhouse S T and Sadeghpour H R 2010 Ultracold giant polyatomic Rydberg molecules: coherent control of molecular orientation *Phys. Rev. Lett.* **104** 243002

[93] Rittenhouse S T, Mayle M, Schmelcher P and Sadeghpour H R 2011 Ultralong-range polyatomic Rydberg molecules formed by a polar perturber *J. Phys. B: At. Mol. Opt. Phys.* **44** 184005

[94] Mayle M, Rittenhouse S T, Schmelcher P and Sadeghpour H R 2012 Electric field control in ultralong-range triatomic polar Rydberg molecules *Phys. Rev.* A **85** 052511

[95] González-Férez R, Sadeghpour H R and Schmelcher P 2015 Rotational hybridization and control of alignment and orientation in triatomic ultralong-range Rydberg molecules *New J. Phys.* **17** 013021

[96] González-Férez R, Rittenhouse S T, Schmelcher P and Sadeghpour H R 2020 A protocol to realize triatomic ultralong range Rydberg molecules in an ultracold KRb gas *J. Phys. B: At. Mol. Opt. Phys.* **53** 074002

[97] González-Férez R, Shertzer J and Sadeghpour H R 2021 Ultralong-range Rydberg bimolecules *Phys. Rev. Lett.* **126** 043401

[98] J T Devreese and F Peeters ed 1984 *Polarons and Excitons in Polar Semiconductors and Ionic Crystals*, (Plenum Press)

[99] Watanabe S, Ando K, Kang K, Mooser S, Vaynzof Y, Kurebayashi H, Saitoh E and Sirringhaus H 2014 Polaron spin current transport in organic semiconductors *Nat. Phys.* **10** 308

[100] Schmidt R, Enss T, Pietilä V and Demler E 2012 Fermi polarons in two dimensions *Phys. Rev.* A **85** 021602

[101] Sidler M, Back P, Cotlet O, Srivastava A, Fink T, Kroner M, Demler E and Imamoglu A 2017 Fermi polaron-polaritons in charge-tunable atomically thin semiconductors *Nat. Phys.* **13** 255

[102] Massignan P, Zaccanti M and Bruun G M 2014 Polarons, dressed molecules and itinerant ferromagnetism in ultracold Fermi gases *Rep. Prog. Phys.* **77** 034401

[103] Hu M-G, Van de Graaff M J, Kedar D, Corson J P, Cornell E A and Jin D S 2016 Bose polarons in the strongly interacting regime *Phys. Rev. Lett.* **117** 055301

[104] Jørgensen N B, Wacker L, Skalmstang K T, Parish M M, Levinsen J, Christensen R S, Bruun G M and Arlt J J 2016 Observation of attractive and repulsive polarons in a Bose-Einstein condensate *Phys. Rev. Lett.* **117** 055302

[105] Schirotzek A, Wu C-H, Sommer A and Zwierlein M W 2009 Observation of Fermi polarons in a tunable Fermi liquid of ultracold atoms *Phys. Rev. Lett.* **102** 230402

[106] Kohstall C, Zaccanti M, Jag M, Trenkwalder A, Massignan P, Bruun G M, Schreck F and Grimm R 2012 Metastability and coherence of repulsive polarons in a strongly interacting Fermi mixture *Nature* **485** 615

[107] Koschorreck M, Pertot D, Vogt E, Fröhlich B, Feld M and Köhl M 2012 Attractive and repulsive Fermi polarons in two dimensions *Nature* **485** 619

[108] Hunter A L, Eiles M T, Eisfeld A and Rost J M 2020 Rydberg composites *Phys. Rev.* X **10** 031046

[109] Eiles M T, Eisfeld A and Rost J M 2023 Anderson localization of a Rydberg electron *Phys. Rev. Res.* **5** 033032

[110] Durst A A T and Eiles M T 2024 Phenomenology of a Rydberg impurity in an ideal Bose Einstein condensate *Phys. Rev. Res.* accepted

[111] Tiwari S, Engel F, Wagner M, Schmidt R, Meinert F and Wüster S 2022 Dynamics of atoms within atoms *New J. Phys.* **24** 073005

[112] Sous J, Sadeghpour H R, Killian T C, Demler E and Schmidt R 2020 Rydberg impurity in a fermi gas: quantum statistics and rotational blockade *Phys. Rev. Res.* **2** 023021

[113] Karpiuk T, Brewczyk M, Rzażewski K, Gaj A, Balewski J B, Krupp A T, Schlagmueller M, Löw R, Hofferberth S and Pfau T 2015 Imaging single Rydberg electrons in a Bose–Einstein condensate *New J. Phys.* **17** 053046

[114] Schmidt R, Sadeghpour H R and Demler E 2016 Mesoscopic Rydberg impurity in an atomic quantum gas *Phys. Rev. Lett.* **116** 105302

[115] Gievers M, Wagner M and Schmidt R 2024 Probing polaron clouds by Rydberg atom spectroscopy *Phys. Rev. Lett.* **132** 053401

[116] Wang J, Liu X-J and Hui H 2022 Exact quasiparticle properties of a heavy polaron in BCS Fermi superfluids *Phys. Rev. Lett.* **128** 175301

[117] Wang J, Liu X-J and Hui H 2022 Heavy polarons in ultracold atomic Fermi superfluids at the BEC-BCS crossover: formalism and applications *Phys. Rev.* A **105** 043320

[118] Engel F, Tiwari S K, Pfau T, Wüster S and Meinert F 2024 In situ observation of chemistry in Rydberg molecules within a coherent solvent *Phys. Rev. Res.* **6** 033150
[119] Butscher B, Bendkowsky V, Nipper J, Balewski J B, Kukota L, Löw R, Pfau T, Li W, Pohl T and Rost J M 2011 Lifetimes of ultralong-range Rydberg molecules in vibrational ground and excited states *J. Phys. B: At. Mol. Opt. Phys.* **44** 184004
[120] Coté R and Dalgarno A 2000 Ultracold atom-ion collisions *Phys. Rev.* A **62** 012709
[121] Grier A T, Cetina M, Oručević F and Vuletić V 2009 Observation of cold collisions between trapped ions and trapped atoms *Phys. Rev. Lett.* **102** 223201
[122] Geppert P, Althön M, Fichtner D and Ott H 2021 Diffusive-like redistribution in state-changing collisions between Rydberg atoms and ground-state atoms *Nat. Commun.* **12** 3900
[123] Camargo F, Whalen J D, Ding R, Sadeghpour H R, Yoshida S, Burgdörfer J, Dunning F B and Killian T C 2016 Lifetimes of ultra-long-range strontium Rydberg molecules *Phys. Rev.* A **93** 022702
[124] Whalen J D, Camargo F, Ding R, Killian T C, Dunning F B, Pérez-Ríos J, Yoshida S and Burgdörfer J 2017 Lifetimes of ultralong-range strontium Rydberg molecules in a dense Bose-Einstein condensate *Phys. Rev.* A **96** 042702
[125] Kanungo S K, Whalen J D, Lu Y, Killian T C, Dunning F B, Yoshida S and Burgdörfer J 2020 Loss rates for high-n, $49 \lesssim n \lesssim 150$, $5sns\ (^3s_1)$ Rydberg atoms excited in an ^{84}Sr Bose-Einstein condensate *Phys. Rev.* A **102** 063317
[126] Eustice S, Cassella K and Stamper-Kurn D 2020 Laser cooling of transition-metal atoms *Phys. Rev.* A **102** 053327
[127] Aikawa K, Frisch A, Mark M, Baier S, Rietzler A, Grimm R and Ferlaino F 2012 Bose-Einstein condensation of erbium *Phys. Rev. Lett.* **108** 210401
[128] Lu M, Burdick N Q, Ho Youn S and Lev B L 2011 Strongly dipolar Bose-Einstein condensate of dysprosium *Phys. Rev. Lett.* **107** 190401
[129] Gross C and Bloch I 2017 Quantum simulations with ultracold atoms in optical lattices *Science* **357** 995
[130] Andersen M F 2022 Optical tweezers for a bottom-up assembly of few-atom systems *Adv. Phys.* X **7** 2064231
[131] Ruggiero P, Calabrese P, Doyon B and Dubail J 2021 Quantum generalized hydrodynamics of the Tonks-Girardeau gas: density fluctuations and entanglement entropy *J. Phys. A: Math. Theor.* **55** 024003